2D Transition Metal Dichalcogenide Heterostructures for p- and n-Type Photovoltaic Self-Powered Gas Sensor

Youngjun Kim, Sangyoon Lee, Jeong-Gyu Song, Kyung Yong Ko, Whang Je Woo, Suk Woo Lee, Minwoo Park, Hoonkyung Lee, Zonghoon Lee, Hyunyong Choi, Woo-Hee Kim,* Jusang Park,* and Hyungjun Kim*

2D transition metal dichalcogenides (TMDs) have attracted much attention for their gas sensing applications due to their superior responsivity at typical room temperature. However, low power consumption and reliable selectivity are the two main requirements for gas sensors to be applicable in future electronic devices. Herein, a p-type (WSe_2/WS_2) and n-type (MoS_2/WSe_2) photovoltaic self-powered gas sensor is demonstrated using 2D TMD heterostructures for the first time. The gas sensors are operated by the photovoltaic effect of 2D TMD heterostructures, which are uniformly synthesized by the vacuum-based synthesis. The gas sensing properties of the WSe_2/WS_2 and MoS_2/WSe_2 heterostructure gas sensors are investigated for NO_2 and NH_3 with changing gas concentration, and each sensor exhibits selectivity to NO_2 and NH_3. From the results, it is confirmed that the 2D TMD heterostructures can be a viable platform for highly sensitive, selective gas sensor applications without external bias due to their photovoltaic features. Further, this study contributes toward revealing the gas sensor mechanism in 2D TMD heterostructure.

Dr. Y. Kim, S. Lee, Dr. J.-G. Song, Dr. K. Y. Ko, W. J. Woo, Dr. J. Park, Prof. H. Kim
School of Electrical and Electronic Engineering
Yonsei University
50 Yonsei-Ro, Seodaemun-Gu, Seoul 03722, Republic of Korea
E-mail: jusang@yonsei.ac.kr; hyungjun@yonsei.ac.kr
S. W. Lee, Prof. Z. Lee
School of Materials Science and Engineering
Ulsan National Institute of Science and Technology (UNIST)
50 UNIST-gil, Ulsan 44919, Republic of Korea
M. Park, Prof. H. Lee
Department of Physics
Konkuk University
120 Neungdong-ro, Gwangjin-gu, Seoul 05029, Republic of Korea
Prof. H. Choi
Department of Physics and Astronomy
Seoul National University
1, Gwanak-ro, Gwanak-gu, Seoul 08826, Republic of Korea
Prof. W.-H. Kim
Department of Materials Science and Chemical Engineering
Hanyang University
55, Hanyangdaehak-ro, Sangnok-gu, Ansan-si
Gyeonggi-do 15588, Republic of Korea
E-mail: wooheekim@hanyang.ac.kr

The ORCID identification number(s) for the author(s) of this article can be found under https://doi.org/10.1002/adfm.202003360.

1. Introduction

Gas sensing technologies have recently drawn much attention due to the significantly increasing threats of industrial chemicals as well as daily air pollution caused by exhaust gases from automobiles, huge power plants, etc.[1–3] For daily monitoring and control of unpredictable types and concentrations of toxic gas, the need for highly selective and sensitive gas sensors has become increasingly important. In particular, semiconductor gas sensors have been considered as a prospective candidate for future gas sensor networks due to their simple sensing mechanism, which is based on resistance/current changes upon gas exposure.[4,5]

However, low power consumption and reliable selectivity are the two main requirements for gas sensors to be applicable in future electronic devices. Connected Internet of things (IoTs) devices (e.g., smart phones and wireless sensor platforms) will facilitate personalized detection of environmental conditions, making them the basis of the future core technology of ubiquitous sensing.[6,7] Therefore, recent works have demonstrated promising concepts for realizing self-powered gas sensors that are capable of detecting gases without the need for external power sources to activate the sensor–gas interaction or to actively generate a read-out signal.[8,9] These sensors consume drastically less power than conventional semiconductor gas sensors, and they reduce the required space for integration.

Since 2D transition metal dichalcogenides (TMDs) are promising semiconducting materials as an electronic device for low power consumption and have sensitive gas detection properties at room temperature,[10–12] various studies on 2D TMD-based gas sensing devices have been reported.[13–16] Furthermore, 2D TMD heterostructure, such as MoS_2/WSe_2, has photovoltaic properties with open-circuit voltage (V_{oc}) of 0.2–0.5 V, implying that atomically thin 2D TMD heterostructure could be used for photovoltaic self-powered gas sensors at typical room temperatures under white light illumination.[17,18]

Nevertheless, photovoltaic self-powered gas sensor using 2D TMD heterostructure has not yet been reported. This might be due to the difficulty in achieving a vertically stacked structure, which only one material is exposed to the surface. As 2D TMD

**ADVANCED
SCIENCE NEWS**
www.advancedsciencenews.com

**ADVANCED
FUNCTIONAL
MATERIALS**
www.afm-journal.de

have different responsivity to gases, gas selectivity could be achieved only if they are vertically stacked. Note that most of 2D TMD heterostructures have been fabricated by the exfoliation or chemical vapor deposition (CVD), which inevitably exposes both TMD materials to air, which are not a suitable structure to secure gas selectivity.[17–22]

Herein, we have demonstrated a photovoltaic self-powered gas sensor through the 2D TMD heterostructures for the first time. Vertically stacked WSe_2/WS_2 and MoS_2/WSe_2 heterostructures were fabricated to the gas sensor and operated under white light illumination condition. The gas sensing experiments were performed using NO_2 and NH_3, which were representative electron acceptor and donor molecules, respectively.[12,14–16] Note that both 2D TMD heterostructures were synthesized by the vacuum-based synthesis for large-area uniformity.[15,23–25] For p-type surface, the WSe_2/WS_2 was synthesized by in situ CVD and one transfer process was required. The n-type surface of MoS_2/WSe_2 was synthesized by ex situ process and fabricated as a gas sensor using lithography to ensure its integration. In each gas sensor, only the WSe_2 and MoS_2 were exposed to the surface, respectively, and fabrication methods are suitable for demonstrating the photocurrent without external voltage due to photovoltaic characteristics. The WSe_2/WS_2 gas sensor presented the p-type behavior and selectivity to NO_2 gas. On the other hand, MoS_2/WSe_2 gas sensor showed the n-type gas sensing characteristic and responsivity to NH_3 gas was higher than the NO_2 gas. We found that the exposed surface plays the most dominant role in transferring the charges from the gas, even at monolayer thickness. Further, it was confirmed that the underneath layer could affect the responsivity depending on the type of the heterostructure material and exposed gas through computational research.

2. Results and Discussion

Two different methods were used to implement the photovoltaic self-powered gas sensors using 2D TMD heterostructures. The first process was for the fabrication of the WSe_2/WS_2 heterostructure gas sensor. WSe_2, which is a p-type material, was exposed to the surface for p-type cell, and WS_2, which is an n-type material, was located under the WSe_2 layer.[15,16,25] We attempted to form a heterostructure with few-layer thickness in each layers because the photovoltaic effect became too low in a monolayer/monolayer heterostructure due to the decreased light absorption.[17,19] On the contrary, if the thickness is too thick, it is difficult to use gas sensor at typical room temperatures because of a slow recovery rate.[26,27] The uniform WSe_2/WS_2 was prepared by the in situ synthesis. It was composed of consecutive two-step CVD process for synthesizing centimeter-scale uniform WS_2 and WSe_2, respectively.[15,25] Atomic force microscopy (AFM) height profile analysis of the as-deposited WS_2 and the WSe_2/WS_2 heterostructure was implemented to measure the thickness and surface morphologies. Each sample was transferred onto a bare SiO_2/Si substrate. The thickness of WS_2 was ≈2.2 nm, indicating a trilayer (3L) (**Figure 1**a), and the overall thickness of the WSe_2/WS_2 heterostructure was ≈4.5 nm (Figure 1b), indicating the additional 3L WSe_2 on the 3L WS_2. And, smooth surface could be identified

by the AFM images (Figure 1a,b). The synthesized WSe_2, WS_2, and WSe_2/WS_2 heterostructure were thoroughly examined by Raman spectroscopy, as shown in Figure 1c. WSe_2 presented the Raman spectrum bands at E^1_{2g} and A_{1g} modes from in-plane and out-of-plane vibrations at ≈250 and 258 cm^{-1}, respectively (yellow line), while WS_2 exhibited in-plane E^1_{2g} and out-of-plane A_{1g} modes at ≈350 and 419 cm^{-1}, respectively (purple line).[24,28] In the Raman spectra for the WSe_2/WS_2 heterostructure, the main peaks for WSe_2 and WS_2 are represented as the red line. There was no spectrum of secondary phases such as WS_xSe_{2-x} (alloy formation) causing A_{1g} mode at 380 cm^{-1}.[29–31] This confirmed that the WSe_2/WS_2 heterostructure was successfully formed through the in situ CVD synthesis process.

To further investigate the structure and composition of the WSe_2/WS_2 heterostructure, transmission electron microscopy (TEM) was conducted, as shown in Figure 1d. The cross-sectional TEM image clearly presents the formation of the vertically stacked heterostructure. A distinguishable layer structure evidently verifies the layer-by-layer growth for monolithic configuration with the precise control by the in situ CVD. In addition, the whole structure consisting of 3L for each WSe_2 and WS_2 material was consistent with the AFM height analysis. Moreover, the energy-dispersive X-ray spectroscopy (EDS) mapping images in Figure 1e–h and high angle annular dark field (HAADF) image in Figure S1b in the Supporting Information further confirm the elemental composition of the vertical WSe_2/WS_2 heterostructure. W atoms were well distributed across the entire heterostructure, while S and Se atoms were clearly distinguishable in the separated layered structure. From those measurements, the synthesized WSe_2/WS_2 showed the layer-by-layer CVD growth with highly controlled thickness, eventually achieving a vertically stacked heterostructure. As presented in Figure S1c,d in the Supporting Information, the high-resolution top-view image TEM and the selected area electron diffraction pattern (SAED) exhibit the polycrystalline structures of the synthesized WSe_2/WS_2 heterostructure. The grain size was measured to be ≈30 nm.

Based on the vertically stacked WSe_2/WS_2 heterostructure, the gas sensor was fabricated with bottom (Au) and top (Pd) electrodes, as depicted in Figure 1i. This structure was designed to contact the electrodes with WSe_2 and WS_2, respectively, and only expose the WSe_2 surface to the gases. A photograph of the completely fabricated WSe_2/WS_2 gas sensor is shown in Figure 1j. The optical microscopy (OM) images in Figure S1e–g in the Supporting Information show the successive fabrication processes of uniform WSe_2/WS_2 gas sensor from the bottom electrode patterning to the top electrode patterning.

Next to the p-type surface heterostructure, a self-powered gas sensor with n-type surface, MoS_2/WSe_2 heterostructure, was fabricated. We synthesized the MoS_2 and WSe_2 as n-type and p-type materials using previously developed vacuum-based synthesis processes, respectively.[23,24] In this study, 3L WSe_2 on SiO_2 was synthesized by a self-limiting layer synthesis and monolayer (1L) MoS_2 was subsequently synthesized on 3L WSe_2.[23,24] The 1L MoS_2 and 3L WSe_2 served sufficient light absorption thickness for photovoltaic effect.[17,32] Note that vertically stacked MoS_2 and WSe_2 layers with wafer-scale uniformity were confirmed to have n-type and p-type, respectively, in terms of their field-effect transistor (FET) characteristics.[23,24]
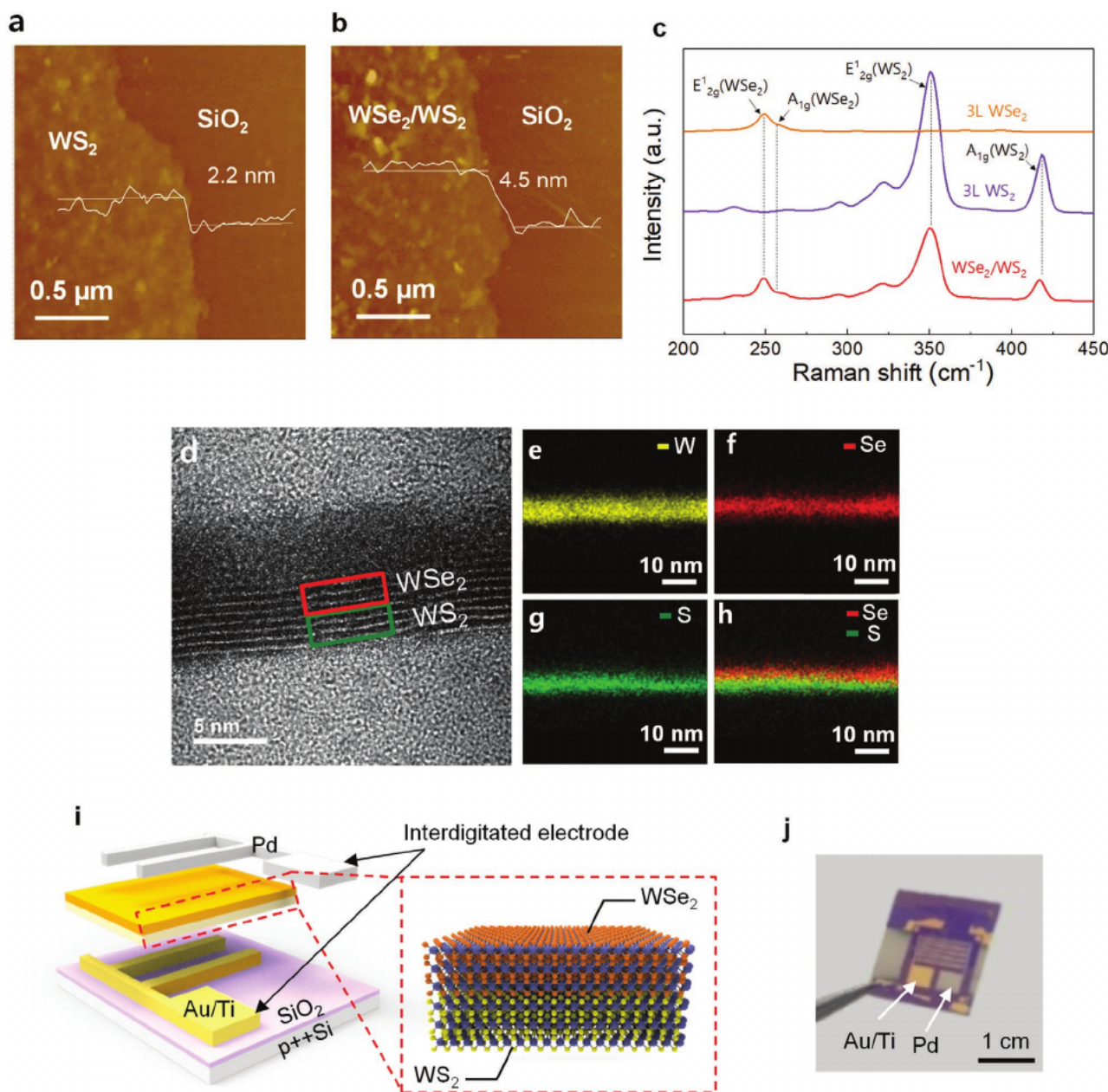
ADVANCED
SCIENCE NEWS

www.advancedsciencenews.com

ADVANCED
FUNCTIONAL
MATERIALS

www.afm-journal.de

Figure 1. AFM image and height profile of a) WS_2 and b) WSe_2/WS_2 heterostructure. c) Raman spectra for WSe_2/WS_2 heterostructure with WSe_2 and WS_2. d) Cross-sectional TEM image of vertically stacked WSe_2/WS_2 heterostructure. Cross-sectional EDS mapping images indicating e) W atoms, f) Se atoms, g) S atoms, and h) S and Se atoms. i) Schematic of the WSe_2/WS_2 gas sensor. j) Photographic image of the fabricated WSe_2/WS_2 gas sensor.

AFM was used for measuring the thickness of MoS_2/WSe_2 and Raman spectroscopy was employed to confirm whether an alloy was formed between two materials during the synthesis of MoS_2 on WSe_2.[32] **Figure 2**a,b shows AFM height profile analysis images of transferred 3L WSe_2 and 1L MoS_2/3L WSe_2 on the SiO_2 substrate. The thickness was 3 nm, which corresponds to four layers (4L) of 2D TMDs.[33] Figure 2c shows the Raman spectra for 1L MoS_2/SiO_2, 3L WSe_2/SiO_2, and 1L MoS_2/3L WSe_2/SiO_2. E^1_{2g} and A_{1g} Raman peaks for 1L MoS_2/SiO_2 were observed at 383.5 and 403.6 cm^{-1}, respectively, with the peak distance of 20.1 cm^{-1} indicating 1L MoS_2/SiO_2.[23,32] The sum

of the E^1_{2g} and A_{1g} peaks at 249.8 cm^{-1} was observed in the 3L WSe_2/SiO_2. The height ($\approx$2.3 nm) of 3L WSe_2 was measured by AFM, which corresponded to the Raman data.[24] For the 1L MoS_2/3L WSe_2, a 3L WSe_2 peak was observed with peaks for MoS_2 (E^1_{2g} at 378.7 cm^{-1} and A_{1g} at 403.5 cm^{-1}), indicating that MoS_2 was synthesized on the 3L WSe_2. Also, the absence of any Raman peaks related to $MoSe_2$ (E^1_{2g} at 286 cm^{-1} and A_{1g} at 244 cm^{-1}) or WS_2 (E^1_{2g} at 356 cm^{-1} and A_{1g} at 420 cm^{-1}) indicates that there was no significant mixing or alloying phenomena in the MoS_2/WSe_2 heterostructure during the synthesis.[33,34] It should be noted that there was a noticeable 5 cm^{-1} downshift in
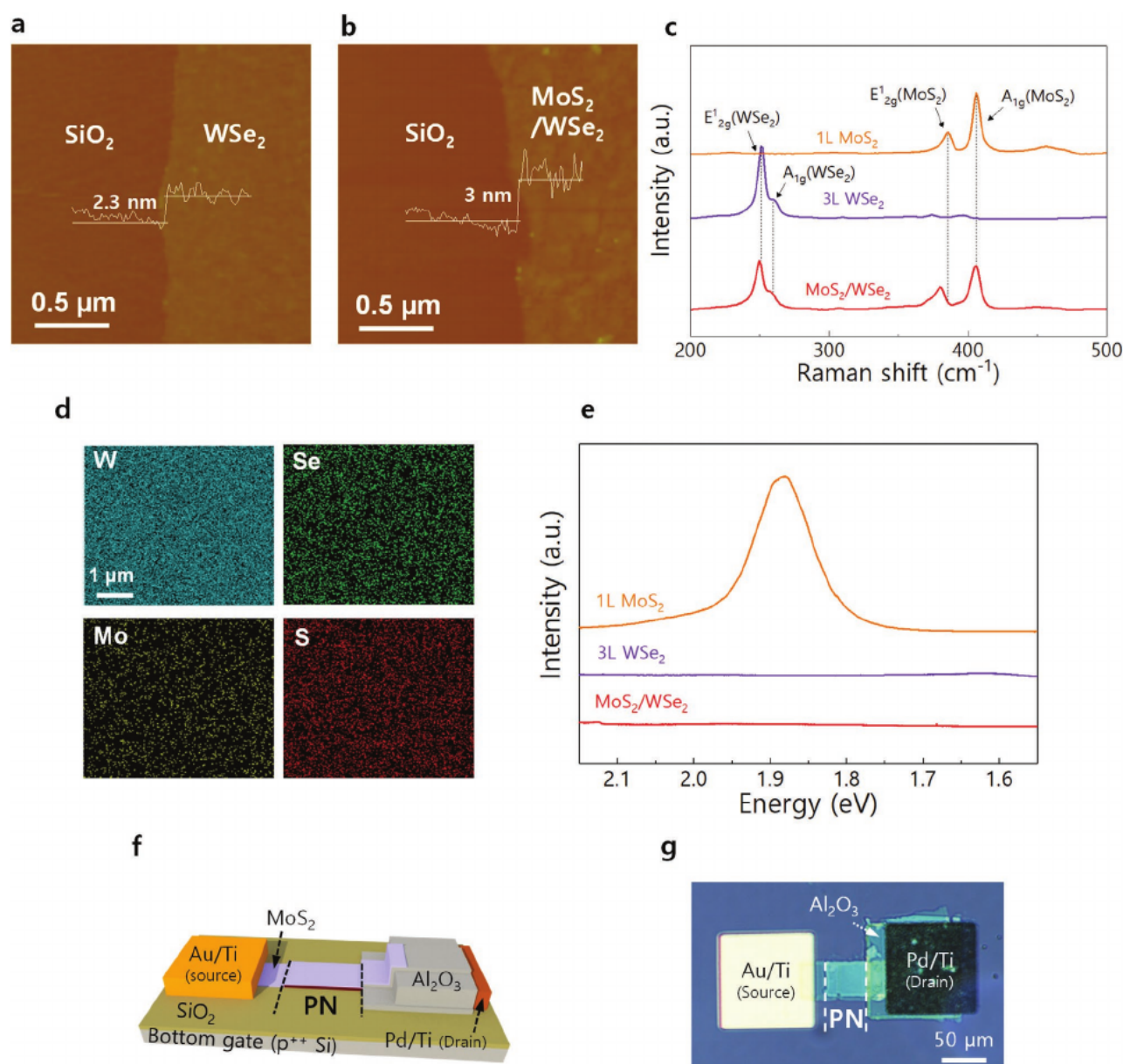
Figure 2. AFM image and height profile of a) WSe_2 and b) MoS_2/WSe_2 c) Raman spectra of 1L MoS_2, 3L WSe_2 and 1L MoS_2/3L WSe_2 heterostructure. d) EDS mapping of MoS_2/WSe_2 heterostructure. e) PL spectra of 1L MoS_2, 3L WSe_2, and 1L MoS_2/3L WSe_2 heterostructure. f) Schematic illustration and g) OM image of fabricated MoS_2/WSe_2 gas sensor.

the E^1_{2g} peak of MoS_2 in the 1L MoS_2/3L WSe_2 region relative to the 1L MoS_2. As reported previously, this is presumably attributed to the interaction between MoS_2 and WSe_2.[32,35] Raman mapping was employed to examine the uniformity of 1L MoS_2 on 3L WSe_2. Figure S2a,b in the Supporting Information shows the Raman mapping on the peak intensity of WSe_2 E^1_{2g} and the intensity ratio of WSe_2 E^1_{2g} and MoS_2 A_{1g}, respectively. The results indicate the uniform synthesis of 1L MoS_2/3L WSe_2. Furthermore, we measured the EDS mapping for the vertically stacked MoS_2/WSe_2, which reveals the uniformly distributed W, Se, Mo, and S elements of WSe_2 and MoS_2 (Figure 2d). Figure 2e presents the photoluminescence (PL) spectra of 1L MoS_2, 3L WSe_2, and 1L MoS_2/3L WSe_2. It was evident that the

strong PL peak for the direct gap transition of 1L MoS_2 was highly suppressed by the WSe_2 layer in MoS_2/WSe_2, which is attributable to the rapid separation of charge carriers.[17,32,35] The schematic illustration and the OM image of the fabricated MoS_2/WSe_2 gas sensor are shown in Figure 2f,g, respectively.

The PN diode characteristics of the fabricated MoS_2/WSe_2 heterostructure were determined because it is closely related to the performance of photovoltaic behavior. The PN diode is dependent on the back-gate voltage, which is adjusted by varying carrier concentration through electrical doping. The calculated forward/reverse current ratio at $V_{ds} = |5 V|$ clearly shows the gate-tunable PN diode characteristics (**Figure 3**a). Additionally, the calculated forward/reverse current ratio (≈560 at $V_g = 10 V$)
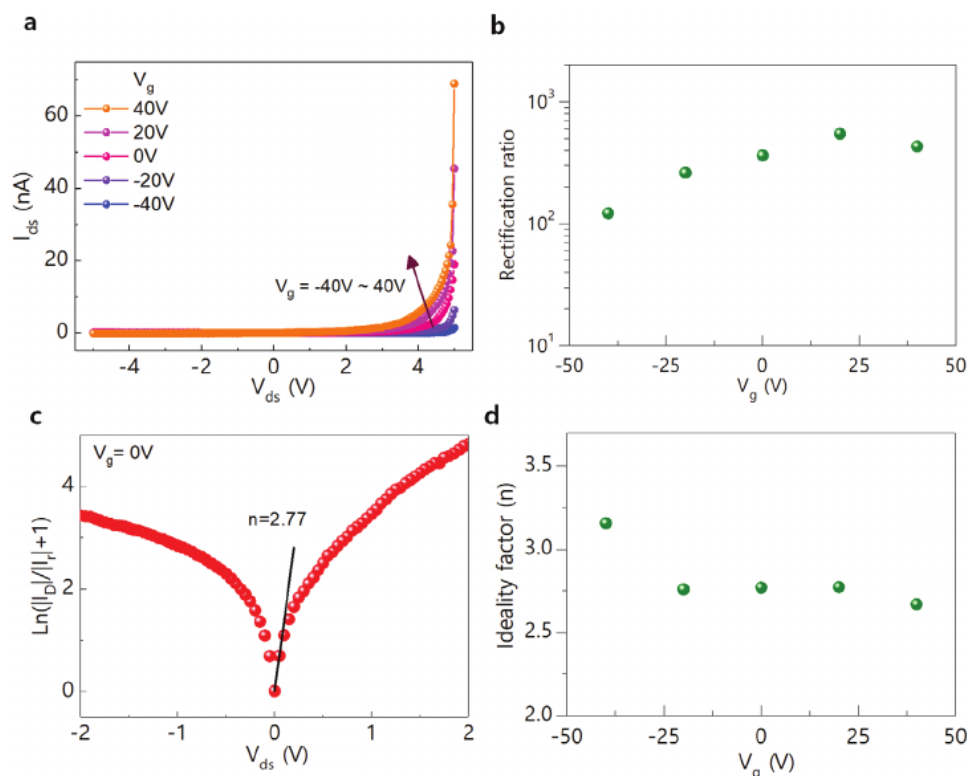
Figure 3. a) *I–V* characteristics of MoS_2/WSe_2 PN diode with gate bias between –40 and 40 V. b) Rectification ratio of the MoS_2/WSe_2 PN diode with gate bias. c) Ideality factor graph of MoS_2/WSe_2 PN diode at V_g = 0 V with V_{ds} between –2 and 2 V. d) Ideality factor depending on back-gate voltage.

was higher than that of a previously reported PN diode based on 1L MoS_2/1L WSe_2 (≈50 at V_{ds} = |8 V| and ≈80 at V_{ds} = |5 V|) (Figure 3b).[36] This gate-tunable characteristic of the PN diode could be explained by a variation in carrier density with electrical doping of the PN rectifying region. Initially, the majority carriers in MoS_2 (electron) and WSe_2 (hole) were depleted under a reverse bias.[36] Under a forward bias, the majority carriers were recombined at an interlayer that can be described by Shockley–Read–Hall and Langevin recombination, as well as the carriers were able to overcome the conduction and the valence band offset, thereby ensuring that a continuous current was maintained.[17,19,21,32,36] With increasing or decreasing gate voltage, p-type WSe_2 was electrically doped to n-type or MoS_2 was depleted, respectively. As a result, a continuous current was maintained regardless of the bias direction. In addition, to determine whether the diode was working ideally, we fitted the Shockley equation

$$|I_D| = |I_{rs}| \left(e^{\frac{eV_D}{nk_BT}} - 1 \right) \tag{1}$$

where I_D is the drain current, V_D is the drain bias, I_{rs} is the reverse saturation current, e is the electronic charge, n is the ideality factor, k_B is the Boltzmann constant, and T is the operation temperature (300 K).[37] The ideal factor was 2.77 with a back-gate voltage of 0 V (Figure 3c), and the value was almost the same for back-gate voltages from –25 to 40 V (Figure 3d). The factor was similar to the PN diode heterostructure with monolayer MoS_2 and black phosphorus by exfoliation, which

we expected that the synthesized MoS_2/WSe_2 heterostructure could produce the photovoltaic effect even if it is synthesized by an ex situ process.[17,38]

By using the above two types of 2D TMD heterostructures, we first checked the photovoltaic effect. **Figure 4**a,b shows schematics of two devices under white light illumination with an incident optical power density of 10 W m^{-2}. The *I–V* curves of the WSe_2/WS_2 (Figure 4c) and the MoS_2/WSe_2 (Figure 4d) heterostructure under light illumination definitely indicate the photovoltaic characteristics. The short-circuit current density and the open-circuit voltage of the WSe_2/WS_2 heterostructure were 0.9 mA m^{-2} and 0.74 mV, respectively. In case of the MoS_2/WSe_2 heterostructure, the short-circuit current density and the open-circuit voltage were 0.45 mA m^{-2} and 25 mV, respectively. Those current densities were lower than the MoS_2/WSe_2 by exfoliation, where the differences between grain size, fabrication process and experimental conditions were assumed to be a reason.[17] In both devices, we found that the current increased with light illumination because of the generation of optically excited carriers. The open-circuit voltage directly indicated a photovoltaic effect. Without light illumination, both 2D TMD heterostructures showed no current at V_{ds} = 0 V. When they were illuminated, electron–hole pairs in both MoS_2/WSe_2 and WSe_2/WS_2 layers were generated, as illustrated in Figure 4e. The schematic energy band diagram in Figure 4e depicts the separation processes of photoexcited charge carriers taking place within the WSe_2/WS_2 and the MoS_2/WSe_2 heterostructures. Here, the electron–hole pairs in both the WSe_2 and WS_2 (MoS_2) layers were photogenerated
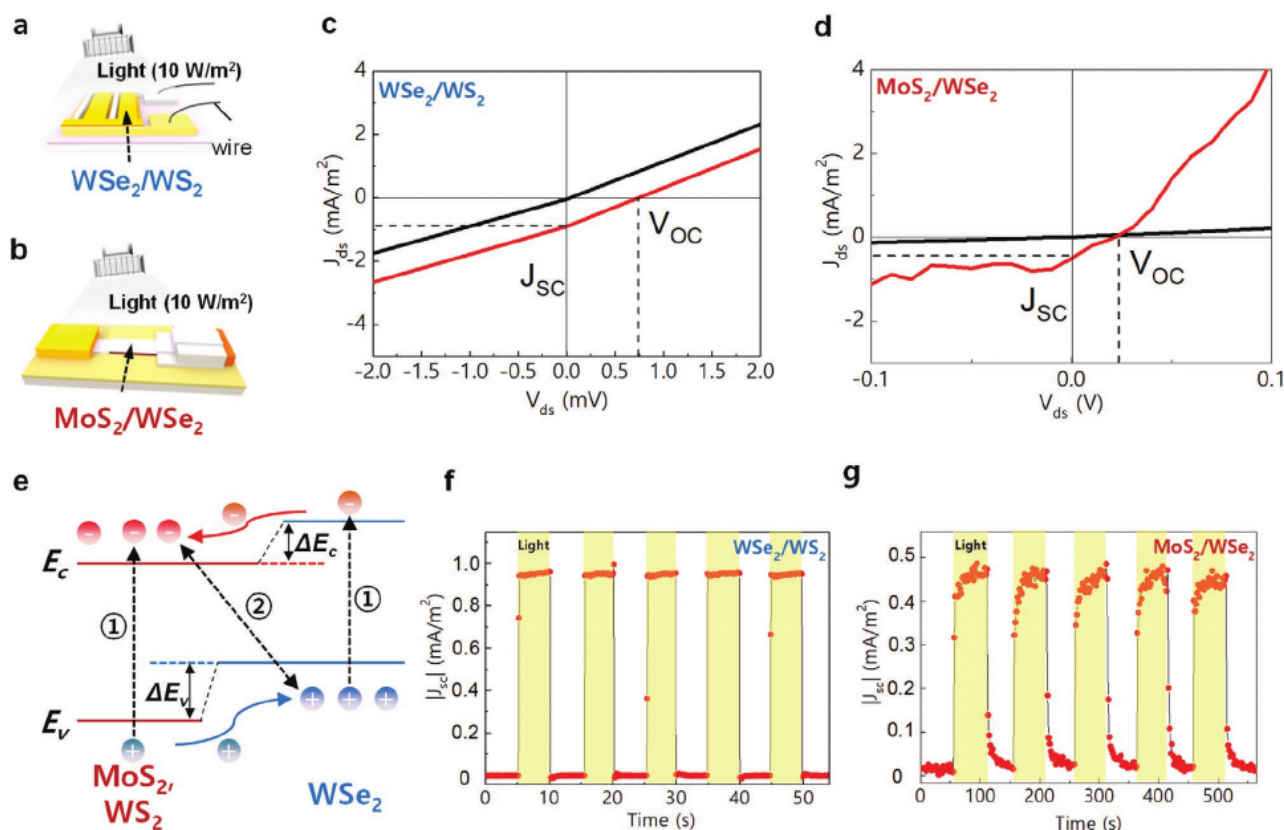
Figure 4. Schematic illustration of light illumination at fabricated a) WSe_2/WS_2 and b) MoS_2/WSe_2 gas sensor. *I–V* characteristics of c) WSe_2/WS_2 and d) MoS_2/WSe_2 gas sensor under each dark/light condition. e) Band energy diagram of 2D TMD heterostructures under light illumination. Photodynamics of f) WSe_2/WS_2 and g) MoS_2/WSe_2 gas sensor with 0 V bias.

because the electrons in the valence band were excited to the conduction band under light illumination. Then, the relaxation of the generated carriers occurred, which was driven by the band offsets ΔE_C and ΔE_V.[36,39] The electrons were diffused to the n-type WS_2 (MoS_2) layers, while the holes were swept into the p-type WSe_2 layers. This charge separation, through the aid of the built-in electric field across the junction, induced further electrical polarization of the heterostructure and eventually acted as a driving force for gas sensing for the WSe_2/WS_2 and MoS_2/WSe_2 heterostructures without the external bias voltage. In addition, the photodynamics of the WSe_2/WS_2 and MoS_2/WSe_2 heterostructures at 0 V bias are presented in Figure 4f,g, respectively. The photocurrent switching under light illumination was operated for five repeats. From those experiments, we confirmed the photovoltaic characteristics of the fabricated 2D TMD heterostructure devices.

Based on the photovoltaic effect, the devices were tested to detect electron acceptor NO_2 gas and electron donor NH_3 gas, in the absence of external bias voltage. Accordingly, the photovoltaic self-powered gas sensing experiments were conducted on WSe_2/WS_2 under light illumination with exposure to NO_2 and NH_3 gases, as illustrated in **Figure 5**a. Upon the exposure to both NO_2 and NH_3, the changes in the photocurrent generated by each gas were observed respectively, as shown in Figure 5b,c. The gas sensing response (%) was calculated using the following equation[13,16]

$$\text{Response (\%)} = \frac{I_g - I_0}{I_0} \times 100\% = \frac{\Delta I}{I_0} \times 100\% \qquad (2)$$

where I_0 is the base current, and I_g refers to the corresponding current with the target gas exposure. Figure 5b shows the changes in photocurrent generated by the WSe_2/WS_2 gas sensor upon the NO_2 exposure (concentrations of 10, 20, 50, 100, 200, and 500 ppm). The NO_2 exposure to the WSe_2/WS_2 gas sensor was maintained for 10 min (blue color region in Figure 5b), followed by the inert N_2 gas for desorbing the NO_2 gas (white region in Figure 5b). The positive sensing response by NO_2 gas was observed with a gradual increase in response from 178% (10 ppm) to 322% (500 ppm) And, it showed good recovery at the room temperature compared to previous reports.[10,40]

In contrast, an opposite phenomenon was observed when exposed to NH_3. Figure 5c shows the changes in photocurrent of the WSe_2/WS_2 gas sensor upon the exposure to NH_3 (concentrations of 10, 20, 50, 100, 200, and 500 ppm). The exposure to NH_3 was also maintained for 10 min, followed by the N_2 purging. Then, the photocurrent level decreased with the NH_3 exposure. The increase in concentration of NH_3 gas up to 500 ppm led to the negative sensing response, gradually decreasing from −19% (10 ppm) to −23% (500 ppm) (Figure 5c). This indicates that the WSe_2/WS_2 gas sensor is useful for the NO_2 gas, compared to the NH_3 gas.
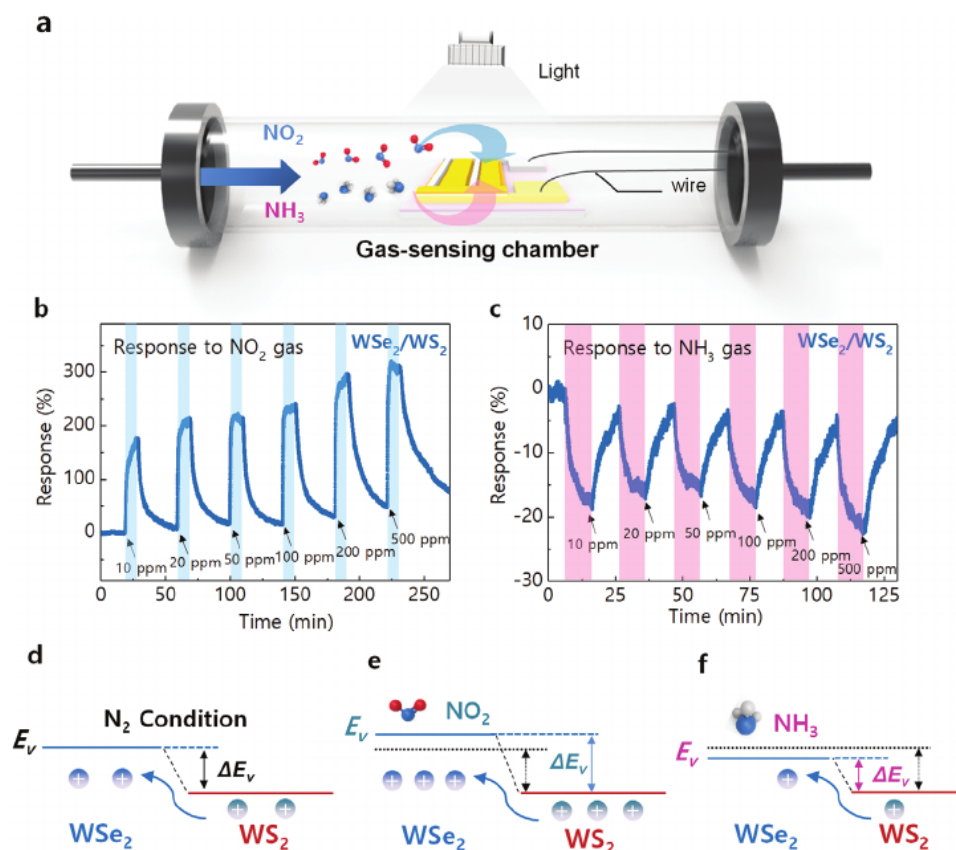
Figure 5. a) Schematic illustration of WSe$_2$/WS$_2$ gas sensor for NO$_2$ and NH$_3$. Consecutive measurement of b) NO$_2$ and c) NH$_3$ gas sensing. Charge transfer process at d) N$_2$ condition, and band bending under e) NO$_2$ and f) NH$_3$ gas exposure at WSe$_2$/WS$_2$ gas sensor.

The gas sensing characteristics of 2D TMD were based on the charge-transfer mechanism induced by the physisorption of gas molecules mostly over pristine surface areas of the 2D TMDs.[41,42] When the NO$_2$ gas was injected, the adsorption of NO$_2$ molecules acted as an electron acceptor and extracted electrons from the adjacent WSe$_2$ layer, thereby increasing hole concentrations. From that, the valence band of the WSe$_2$ layer with the adsorption of NO$_2$ molecules increased compared to the N$_2$ condition, as depicted in Figure 5d,e (dotted line: before gas adsorption; solid line: after gas adsorption). This eventually led to an increase in photocurrent compared with the case of the N$_2$ condition, as shown in Figure 5b. On the other hand, the adsorption of NH$_3$ molecules on the WSe$_2$ layer induced a decrease in hole concentrations due to the role as electron donors (Figure 5f).[16,43] Therefore, we observed a decrease in photocurrent in the WSe$_2$/WS$_2$ gas sensor as in Figure 5c.

We further measured the V_{oc} changes for each gas sensing (Figure S4, Supporting Information) and found a correspondence with the following ideal p–n heterostructure solar diode equation[44]

$$V_{OC} = \frac{KT}{q} \ln \left(\frac{I_{ph}}{I_{rev,sat}} + 1 \right) \tag{3}$$

where K is the Boltzmann constant, q is charge, I_{ph} is photocurrent generated by light illumination, and $I_{rev,sat}$ is reverse saturation current. Here, because $I_{rev,sat}$ can be considered as a

negligible factor with a constant value, the increasing hole concentrations from the NO$_2$ exposure induced the increment of V_{oc} (Figure S5c, Supporting Information). On the other hand, the decreasing hole concentrations due to the NH$_3$ exposure led to a reduction in V_{oc} (Figure S5d, Supporting Information). From these measurements, we were able to understand the changes in the photovoltaic characteristics in terms of the charge-transfer mechanism between the injected gas molecules and the surface of 2D TMD heterostructure under light illumination.

Similarly, we conducted the gas sensing experiments on the MoS$_2$/WSe$_2$ for NO$_2$ and NH$_3$ gas, as shown in **Figure 6**a. Figure 6b presents the calculated gas sensing response of the MoS$_2$/WSe$_2$ gas sensor upon the NO$_2$ exposure (concentrations of 50, 100, 200, and 500 ppm). The MoS$_2$/WSe$_2$ gas sensor was exposed to the NO$_2$ for 5 min, and then it was purged in N$_2$ gas for 5 min for recovery. In MoS$_2$/WSe$_2$ gas sensor, we shortened the response time to 5 min because it is sufficient for NO$_2$ gas response saturation. In this case, NO$_2$ gas mainly adsorbed on the n-type MoS$_2$ surface and acted as an electron acceptor (Figure 6e), and the responsivity range was ≈−15% (50 ppm) to −36% (500 ppm).

Figure 6c shows the current change of the MoS$_2$/WSe$_2$ gas sensor upon the NH$_3$ exposure (concentrations of 10, 20, 50, 200, and 500 ppm). The MoS$_2$/WSe$_2$ was exposed to NH$_3$ gas for 5 min and then purged with N$_2$ for 5 min, which are the same time for NO$_2$ gas. As NH$_3$ molecules acted as electron
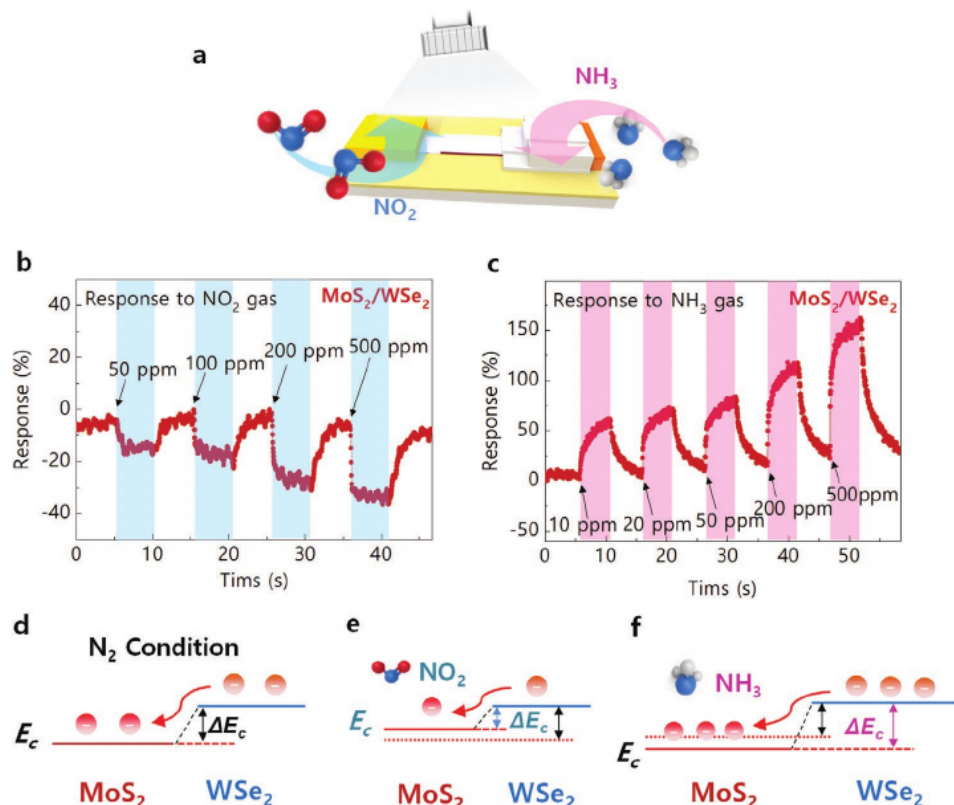
**ADVANCED
SCIENCE NEWS**

www.advancedsciencenews.com

**ADVANCED
FUNCTIONAL
MATERIALS**

www.afm-journal.de

Figure 6. a) Schematic illustration of MoS_2/WSe_2 gas sensor for NO_2 and NH_3. Consecutive measurement of b) NO_2 and c) NH_3 gas sensing. Charge transfer process at d) N_2 condition, and band bending under e) NO_2 and f) NH_3 gas exposure at MoS_2/WSe_2 gas sensor.

donors, the electron concentration of MoS_2 increased, as shown in Figure 6f.[14,42] Therefore, the electron concentration increased in the MoS_2 layer, rising the photocurrent. Then, the photocurrent response of the MoS_2/WSe_2 gas sensor resulted in a positive sensing response, increased from 62% (10 ppm) to 165% (500 ppm), which is much higher than that for NO_2 gas. This tendency was entirely opposite to the case of the WSe_2/WS_2 gas sensor.

The responsivities of the NO_2 and NH_3 gases for each gas sensor are presented in **Figure 7**a,b, respectively. Based on this comparative analysis of gas sensing responsivity between

WSe_2/WS_2 and MoS_2/WSe_2 heterostructures, we found that the exposed surface plays the most dominant role in transferring the charges from the gas, even at monolayer thickness.

To identify and interpret the observed difference in responsivity of surface material with gas molecules, we performed first-principles calculations based on the adsorption of gas molecules on 2D TMDs (**Figure 8**). According to the calculation results, NH_3 gives electrons to the 2D TMD layers, while NO_2 receives electrons. In other words, NH_3 acts like an n-type dopant and NO_2 acts like a p-type dopant, as shown in Figure 8, which agree with our experimental results. For a
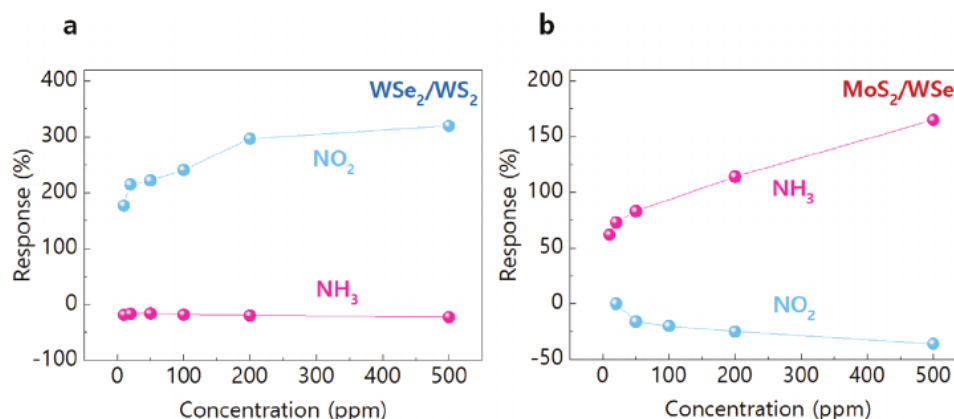

Figure 7. Calculated response of a) WSe_2/WS_2 and b) MoS_2/WSe_2 gas sensor corresponding to each gas concentration of NO_2 and NH_3.
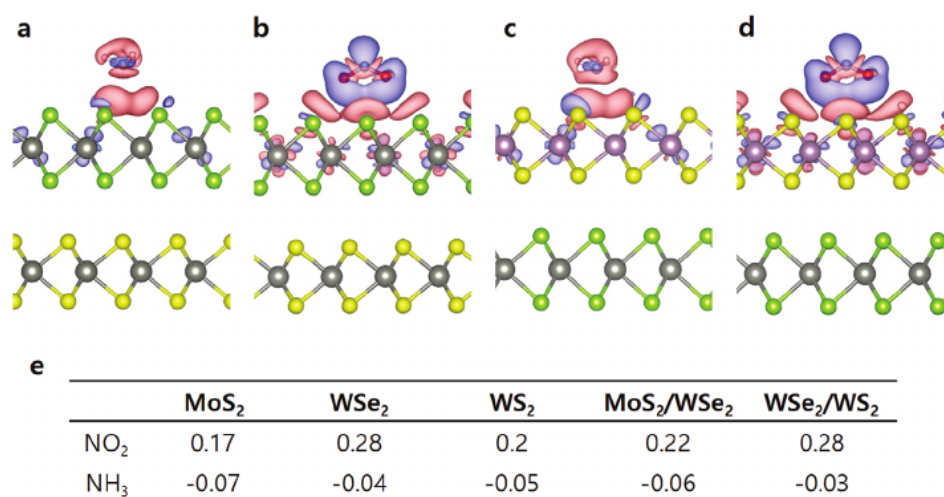
e	MoS₂	WSe₂	WS₂	MoS₂/WSe₂	WSe₂/WS₂
NO₂	0.17	0.28	0.2	0.22	0.28
NH₃	-0.07	-0.04	-0.05	-0.06	-0.03

Figure 8. The difference in the charge densities of a) NH_3 b) NO_2 adsorbed on WSe_2/WS_2 heterostructure, and c) NH_3 d) NO_2 adsorbed on MoS_2/WSe_2 heterostructure, respectively, obtained from DFT calculations. Gray, yellow, green, and purple dots indicate the W, S, Se, and Mo atoms, respectively. Blue and red colors indicate electron accumulation and depletion. e) The calculated transferred charges between the gas molecules and 2D TMD. The unit of the number is the elementary charge, e, and the positive and negative signs indicate the accumulation and depletion of electrons.

single TMD materials in our calculation performed, NO_2 had a larger amount of charge transfer than NH_3, which are similar to previous reports.[42,43] Further, the adsorption energy of NH_3 was smaller than the NO_2 on WSe_2.[43] In addition, even if the number of TMD layer increased, there was little difference in adsorption energy. [27] Therefore, in the 3L WSe_2/3L WS_2 gas sensor, the lower responsivity of NH_3 than that of NO_2 gas is presumably due to the relatively lower adsorption energy and smaller charge transfer ability of NH_3 gas with WSe_2 surface.[15,16,43] On the other hand, it is interesting to note that the lower responsivity to NO_2 than NH_3 in MoS_2/WS_2 gas sensor.[14] In case of MoS_2, the adsorption energies of NH_3 and NO_2 were similar.[42,45] Therefore, the amount of charge transfer between the gas and MoS_2/WSe_2 was crucial for gas sensing responsivity. From the computational simulation results, NO_2 gas had a larger charge transfer value in MoS_2/WSe_2 than in MoS_2. It means that there exists the charge transfer between the NO_2 and the WSe_2 layer.[46] As WSe_2 and MoS_2 behaves in an opposite manner to the NO_2 gas, it was considered that the response of MoS_2/WSe_2 to NO_2 gas was low. In contrast, the degree of charge transfer between the NH_3 and WSe_2 was smaller compared to the case of NO_2. Hence, the MoS_2/WSe_2 gas sensor is more appropriate for detecting the NH_3 gas than NO_2 gas.

In addition, the response and recovery time of the NO_2 sensing (10 ppm) by WSe_2/WS_2 (Figure S6a, Supporting Information) and the NH_3 sensing (10 ppm) by MoS_2/WSe_2 (Figure S6b, Supporting Information) were measured. The response time was measured from the 10% response point to 90% of an end point (maximum), and the recovery time was measured at the point where the current hit the one-tenth point near the minimum from the one-ninth point near the maximum. Consequently, the response and recovery times for the NO_2 detection by the WSe_2/WS_2 gas sensor were determined to be about 387 s (≈6 min) and 728 s (≈12 min), respectively. In the same manner, the time period for one cycle of NH_3 sensing (10 ppm) for MoS_2/WSe_2 was characterized. For the NH_3 detection by the MoS_2/WSe_2 gas sensor, it showed a response time

of ≈205 s (≈3 min) and a recovery time of ≈263 s (≈4 min). The ratio of recovery time to response time by our devices was relatively fast, compared to the previous reports.[14–16,47,48]

3. Conclusion

In summary, we successfully demonstrated a photovoltaic self-powered gas sensor using both WSe_2/WS_2 and MoS_2/WSe_2 heterostructures for the first time. The 2D TMD heterostructures effectively induced separation of photoexcited charge carriers with the built-in electric field under light illumination, which acted as a driving force for gas sensing. The fabricated 2D TMD heterostructure gas sensors showed strong abilities to detect NO_2 and NH_3 gases with high responsivity and selectivity without external bias voltage. The gas sensing mechanism was further elucidated through establishing the correlations of charge transfer with the type of adsorbed gas molecules onto the exposed surface of 2D TMD heterostructure gas sensor. We confirmed that the photovoltaic features of 2D TMD heterostructures could be a viable platform for highly sensitive gas sensor applications. Further, research related to practical gas sensing circumstances such as selective sensing of mixed gas will contribute to a significant advancement in environmental monitoring systems.

4. Experimental Section

Fabrication of WSe_2/WS_2 Heterostructure Gas Sensor: The experimental procedure for the in situ synthesis of the WSe_2/WS_2 heterostructure is illustrated in Figure S1a in the Supporting Information. Tube-type chamber equipment was used for in situ synthesis of the WSe_2/WS_2 heterostructure, as depicted in the schematic image. The SiO_2 (285 nm)/Si substrate was prepared through typical cleaning with acetone, IPA, and deionized water. The tube-type chamber was heated to 700 °C for 30 min. A WS_2 film was deposited on the SiO_2/Si substrate through CVD using tungsten hexachloride (WCl_6) and hydrogen sulfide (H_2S)

gas. Then, the WSe_2 film was synthesized on a WS_2 continuously with WCl_6 and diethyl selenide (DESe) in the same chamber. During both the WS_2 and WSe_2 synthesis steps, the WCl_6 flowed into the chamber with the aid of Ar carrier gas at 50 sccm. Hydrogen (H_2) gas was inserted at 20 sccm during both synthetic processes to prevent unexpected carbon contamination.

The vertically stacked WSe_2/WS_2 heterostructure was fabricated with bottom (Au) and top (Pd) electrodes. After pattering the bottom electrode on a bare SiO_2/Si substrate, the synthesized WSe_2/WS_2 heterostructure was transferred onto the Au/Ti bottom electrode. Finally, Pd (40 nm) was deposited as a top contact. The overall pattern design of the electrodes was formed as an interdigitated electrode.

Fabrication of MoS_2/WSe_2 Heterostructure Gas Sensor: The experimental procedure for the MoS_2/WSe_2 heterostructure as a gas sensor is illustrated in Figure S2c in the Supporting Information. The overall pattern design of the MoS_2/WSe_2 heterostructures and electrodes was formed by conventional lithography with large-area synthesis of 2D TMDs without a transfer method. The SiO_2 (285 nm)/Si substrate was prepatterned by a Pd/Ti electrode (Ti as an adhesion layer) through an evaporation and lift-off method. Then, the WSe_2 was synthesized by a previously reported self-limiting layer (SLS) synthesis method.[24] The tube-type chamber was used to achieve a growth temperature of 700 °C. Tungsten hexachloride (WCl_6) and DESe were used as a precursor and reactant, respectively. The SLS consisted of four steps, each using the same procedure of atomic layer deposition (ALD). A precursor–purge–reactant–purge sequence was repeated for 150 cycles for 3L WSe_2 synthesis. A canister containing the precursor was heated to 90 °C to ensure an adequate vapor pressure for the precursor molecules to be carried into the tube by a pure Ar carrier gas (30 sccm). DESe had sufficient vapor at a typical room temperature (25 °C), so there was no carrier gas injected. In addition, H_2 (10 sccm) gas was injected with DESe during the reactant time. The synthesized WSe_2 was patterned by reactive-ion etching with CHF_3 and O_2 gas for etching gas. Before synthesizing MoS_2 on the WSe_2, Al_2O_3 was deposited by Al (2 nm) evaporation followed by oxidation. Al_2O_3 was patterned by the HNO_3.

The MoS_2 was then synthesized by a catalytic chemical vapor deposition method.[23] MoS_2 was synthesized on prepatterned WSe_2 on the SiO_2 (285 nm)/Si substrate. The tube-type chamber was used to achieve a growth temperature of 700 °C. $MoCl_5$ and dimethyl sulfide (DMS) were used as a precursor and reactant, respectively. The temperature of the canister containing the precursor was heated to 90 °C to achieve adequate vapor pressure, and the vaporized precursor molecules were carried into the tube using Ar carrier gas (3 sccm). The DMS and H_2 flow were fixed at 20 and 10 sccm, respectively. 10 mg of NaCl was added to the hot zone of the CVD reactor, which had a temperature of 700 °C. MoS_2 was etched by reactive-ion etching with CHF_3 and O_2 gas for channel patterning, and Au/Ti was deposited as an electrode to the MoS_2 by evaporation.

Characterization of 2D TMD Heterostructures: OM images were taken using an Olympus DX51, and Raman spectroscopy was performed with a LabRam ARAMIS (HORIBA, 532 nm wavelength laser). AFM was conducted using a multimode scanning microscope (Veeco). Tecnai G2 F20 S-TWIN (accelerating voltage, 80 kV) was employed to characterize the TEM images of the vertically stacked WSe_2/WS_2 heterostructure. A source meter (Keithley 2400) was used to measure the I–V curves, photovoltaic characteristics, and gas sensing properties of the fabricated WSe_2/WS_2 gas sensor. A voltage/current meter (Keithley 4200, Keithley Instruments) was used to measure the I–V curves, photovoltaic characteristics, and gas sensing properties of the fabricated MoS_2/WSe_2 gas sensor.

Gas Sensing Measurement: The whole sensing was implemented at a typical room temperature (25 °C) under white light illumination. The concentration of each gas was set by controlling the flow rate of the target gas and purging gas (N_2) using mass-flow controllers. Basically, the gas sensors were stabilized under N_2 exposure for ≈1 h to blow off moisture, dust, and other particles that could influence the experimental outcome. No external bias was applied to the sensors, and 10 W m^{-2} white light illuminated the sensor with the remainder of the chamber surface covered to block natural light. The real-time output signal (current) was acquired using the source meter mentioned above.

Computational Details: In order to estimate a doping effect on the 2D TMD heterostructure by gas adsorption, the first-principle calculations were performed using density functional theory (DFT) implemented in the Vienna Ab-initio Simulation Package (VASP) with a projector augmented wave (PAW) method.[49] As the exchange–correlation energy functional, the local density approximation (LDA) within the Ceperley–Alder scheme was considered.[50] 2×2 primitive cells of 2D TMD were considered for a unit cell with one gas molecule to theoretical calculations. The kinetic energy cutoff was set to 400 eV. Geometrical optimization for the systems was performed until the Hellmann–Feynman force acting on each atom was smaller than 0.01 eV Å^{-1}. The first Brillouin zone integration was carried out using $9 \times 9 \times 1$ gamma centered grids. The transferred charges between the gas molecules and 2D TMD sheets were calculated using Bader analysis.[42]

Supporting Information

Supporting Information is available from the Wiley Online Library or from the author.

Acknowledgements

Conflict of Interest

The authors declare no conflict of interest.

Keywords

[1] A. Das, R. Dost, T. Richardson, M. Grell, J. J. Morrison, M. L. Turner, *Adv. Mater.* **2007**, *19*, 4018.

[2] S. Ji, H. Wang, T. Wang, D. Yan, *Adv. Mater.* **2013**, *25*, 1755.

[3] J. F. Fernández-Sánchez, I. Fernández, R. Steiger, R. Beer, R. Cannas, U. E. Spichiger-Keller, *Adv. Funct. Mater.* **2007**, *17*, 1188.

[4] W. Tsujita, A. Yoshino, H. Ishida, T. Moriizumi, *Sens. Actuators, B* **2005**, *110*, 304.

**ADVANCED
SCIENCE NEWS**

www.advancedsciencenews.com

**ADVANCED
FUNCTIONAL
MATERIALS**

www.afm-journal.de

[5] S. V. Ryabtsev, A. V. Shaposhnick, A. N. Lukin, E. P. Domashevskaya, *Sens. Actuators, B* **1999**, *59*, 26.

[6] Y. Mo, Y. Okawa, K. Inoue, K. Natukawa, *Sens. Actuators, A* **2002**, *100*, 94.

[7] K. Y. Choi, J. S. Park, K. B. Park, H. J. Kim, H. D. Park, S. D. Kim, *Sens. Actuators, B* **2010**, *150*, 65.

[8] M. W. G. Hoffmann, L. Mayrhofer Dr, O. Casals Dr, L. Caccamo, F. Hernez-Ramirez, G. Lilienkamp, W. Daum, M. Moseler, A. Waag, H. Shen, J. D. Prades, *Adv. Mater.* **2014**, *26*, 8017.

[9] M. W. G. Hoffmann, A. E. Gad, J. D. Prades, F. Hernandez-Ramirez, R. Fiz, H. Shen, S. Mathur, *Nano Energy* **2013**, *2*, 514.

[10] H. Li, Z. Yin, Q. He, H. Li, X. Huang, G. Lu, D. W. H. Fam, A. I. Y. Tok, Q. Zhang, H. Zhang, *Small* **2012**, *8*, 63.

[11] Q. He, Z. Zeng, Z. Yin, H. Li, S. Wu, X. Huang, H. Zhang, *Small* **2012**, *8*, 2994.

[12] S. J. Choi, I. D. Kim, *Electron. Mater. Lett.* **2018**, *14*, 221

[13] K. Y. Ko, J. G. Song, Y. Kim, T. Choi, S. Shin, C. W. Lee, K. Lee, J. Koo, H. Lee, J. Kim, T. Lee, J. Park, H. Kim, *ACS Nano* **2016**, *10*, 9287.

[14] Y. Zhao, J. G. Song, G. H. Ryu, K. Y. Ko, W. J. Woo, Y. Kim, D. Kim, J. H. Lim, S. Lee, Z. Lee, J. Park, H. Kim, *Nanoscale* **2018**, *10*, 9338.

[15] K. Y. Ko, S. Lee, K. Park, Y. Kim, W. J. Woo, D. Kim, J. G. Song, J. Park, J. H. Kim, Z. Lee, H. Kim, *ACS Appl. Mater. Interfaces* **2018**, *10*, 34163.

[16] K. Y. Ko, K. Park, S. Lee, Y. Kim, W. J. Woo, D. Kim, J. G. Song, J. Park, H. Kim, *ACS Appl. Mater. Interfaces* **2018**, *10*, 23910.

[17] C. H. Lee, G. H. Lee, A. M. Van Der Zande, W. Chen, Y. Li, M. Han, X. Cui, G. Arefe, C. Nuckolls, T. F. Heinz, J. Guo, J. Hone, P. Kim, *Nat. Nanotechnol.* **2014**, *9*, 676.

[18] R. Cheng, D. Li, H. Zhou, C. Wang, A. Yin, S. Jiang, Y. Liu, Y. Chen, Y. Huang, X. Duan, *Nano Lett.* **2014**, *14*, 5590.

[19] R. Frisenda, A. J. Molina-Mendoza, T. Mueller, A. Castellanos-Gomez, H. S. J. Van Der Zant, *Chem. Soc. Rev.* **2018**, *47*, 3339.

[20] M. Sun, Q. Fang, D. Xie, Y. Sun, J. Xu, C. Teng, R. Dai, P. Yang, Z. Li, W. Li, Y. Zhang, *Adv. Electron. Mater.* **2017**, *3*, 1600502.

[21] T. Roy, M. Tosun, X. Cao, H. Fang, D. H. Lien, P. Zhao, Y. Z. Chen, Y. L. Chueh, J. Guo, A. Javey, *ACS Nano* **2015**, *9*, 2071.

[22] Y. Xue, Y. Zhang, Y. Liu, H. Liu, J. Song, J. Sophia, J. Liu, Z. Xu, Q. Xu, Z. Wang, J. Zheng, Y. Liu, S. Li, Q. Bao, *ACS Nano* **2016**, *10*, 573.

[23] J. G. Song, G. Hee Ryu, Y. Kim, W. Je Woo, K. Yong Ko, Y. Kim, C. Lee, I. K. Oh, J. Park, Z. Lee, H. Kim, *Nanotechnology* **2017**, *28*, 465103.

[24] K. Park, Y. Kim, J. G. Song, S. J. Kim, C. Wanlee, G. H. Ryu, Z. Lee, J. Park, H. Kim, *2D Mater.* **2016**, *3*, 014004.

[25] J. Park, W. Lee, T. Choi, S. H. Hwang, J. M. Myoung, J. H. Jung, S. H. Kim, H. Kim, *Nanoscale* **2015**, *7*, 1308.

[26] Z. Qin, D. Zeng, J. Zhang, C. Wu, Y. Wen, B. Shan, C. Xie, *Appl. Surf. Sci.* **2017**, *414*, 244.

[27] D. J. Late, Y. K. Huang, B. Liu, J. Acharya, S. N. Shirodkar, J. Luo, A. Yan, D. Charles, U. V. Waghmare, V. P. Dravid, C. N. R. Rao, *ACS Nano* **2013**, *7*, 4879.

[28] W. Zhao, Z. Ghorannevis, K. K. Amara, J. R. Pang, M. Toh, X. Zhang, C. Kloc, P. H. Tan, G. Eda, *Nanoscale* **2013**, *5*, 9677.

[29] M. Zhang, J. Wu, Y. Zhu, D. O. Dumcenco, J. Hong, N. Mao, S. Deng, Y. Chen, Y. Yang, C. Jin, S. H. Chaki, Y. S. Huang, J. Zhang, L. Xie, *ACS Nano* **2014**, *8*, 7130.

[30] Y. Chen, J. Xi, D. O. Dumcenco, Z. Liu, K. Suenaga, D. Wang, Z. Shuai, Y. S. Huang, L. Xie, *ACS Nano* **2013**, *7*, 4610.

[31] X. Duan, C. Wang, Z. Fan, G. Hao, L. Kou, U. Halim, H. Li, X. Wu, Y. Wang, J. Jiang, A. Pan, Y. Huang, R. Yu, X. Duan, *Nano Lett.* **2016**, *16*, 264.

[32] Y. Kim, J. G. Song, Y. J. Park, G. H. Ryu, S. J. Lee, J. S. Kim, P. J. Jeon, C. W. Lee, W. J. Woo, T. Choi, H. Jung, H. B. R. Lee, J. M. Myoung, S. Im, Z. Lee, J. H. Ahn, J. Park, H. Kim, *Sci. Rep.* **2016**, *6*, 18754.

[33] J. G. Song, J. Park, W. Lee, T. Choi, H. Jung, C. W. Lee, S. H. Hwang, J. M. Myoung, J. H. Jung, S. H. Kim, C. Lansalot-Matras, H. Kim, *ACS Nano* **2013**, *7*, 11333.

[34] S. V. Bhatt, M. P. Deshpande, V. Sathe, R. Rao, S. H. Chaki, *J. Raman Spectrosc.* **2014**, *45*, 971.

[35] M. H. Chiu, M. Y. Li, W. Zhang, W. T. Hsu, W. H. Chang, M. Terrones, H. Terrones, L. J. Li, *ACS Nano* **2014**, *8*, 9649.

[36] M. M. Furchi, A. Pospischil, F. Libisch, J. Burgdörfer, T. Mueller, *Nano Lett.* **2014**, *14*, 4785.

[37] D. Jariwala, V. K. Sangwan, C.-C. Wu, P. L. Prabhumirashi, M. L. Geier, T. J. Marks, L. J. Lauhon, M. C. Hersam, *Proc. Natl. Acad. Sci. USA* **2013**, *110*, 18076.

[38] Y. Deng, Z. Luo, N. J. Conrad, H. Liu, Y. Gong, S. Najmaei, P. M. Ajayan, J. Lou, X. Xu, P. D. Ye, *ACS Nano* **2014**, *8*, 8292.

[39] N. Huo, J. Yang, L. Huang, Z. Wei, S. S. Li, S. H. Wei, J. Li, *Small* **2015**, *11*, 5430.

[40] S. Y. Cho, S. J. Kim, Y. Lee, J. S. Kim, W. Bin Jung, H. W. Yoo, J. Kim, H. T. Jung, *ACS Nano* **2015**, *9*, 9314.

[41] C. Zhou, W. Yang, H. Zhu, *J. Chem. Phys.* **2015**, *142*, 214704.

[42] B. Cho, M. G. Hahm, M. Choi, J. Yoon, A. R. Kim, Y. J. Lee, S. G. Park, J. D. Kwon, C. S. Kim, M. Song, Y. Jeong, K. S. Nam, S. Lee, T. J. Yoo, C. G. Kang, B. H. Lee, H. C. Ko, P. M. Ajayan, D. H. Kim, *Sci. Rep.* **2015**, *5*, 8052.

[43] T. Wang, R. Zhao, X. Zhao, Y. An, X. Dai, C. Xia, *RSC Adv.* **2016**, *6*, 82793.

[44] L. Liu, G. H. Li, Y. Wang, Y. Y. Wang, T. Li, T. Zhang, S. J. Qin, *Nanoscale* **2017**, *9*, 18579.

[45] Q. Yue, Z. Shao, S. Chang, L. Jingbo, *Nanoscale Res. Lett.* **2013**, *8*, 425.

[46] G. Liu, S. L. Rumyantsev, C. Jiang, M. S. Shur, A. A. Balandin, *IEEE Electron Device Lett.* **2015**, *36*, 1202.

[47] B. Liu, L. Chen, G. Liu, A. N. Abbas, M. Fathi, C. Zhou, *ACS Nano* **2014**, *8*, 5304.

[48] R. Kumar, N. Goel, M. Kumar, *ACS Sens.* **2017**, *2*, 1744.

[49] D. Joubert, *Phys. Rev. B: Condens. Matter Mater. Phys.* **1999**, *59*, 1758.

[50] D. M. Ceperley, B. J. Alder, *Phys. Rev. Lett.* **1980**, *45*, 566.